

**Fig. 1.** *C/CRY4* photochemistry. (A) CRY proteins exist in an inactive  $FAD^{\bullet-}$  ground state. Absorption of UV or blue light promotes electron transfer from a Trp residue that propagates through the Trp-tetrad to form a  $[FAD^{\bullet-} TrpH^{\bullet+}]$  radical pair. The radical pair undergoes magnetically sensitive singlet-triplet interconversion (mechanism 1 [M1]) in which only the singlet state can recombine to form  $FAD^{\bullet-}$ . Both states can proceed to the  $FADH^{\bullet}$  state, which can either be further reduced or form a second radical pair. The  $[FADH^{\bullet} O_2^{\bullet-}]$  radical pair can also form via reoxidation of  $FADH^{\bullet}$  and can undergo singlet-triplet mixing, in which the singlet state can return to  $FAD^{\bullet-}$  following release of hydrogen peroxide. The M2 mechanism alone is unlikely, due to the fast spin relaxation of superoxide. (B) *C/CRY4* spectra in the dark ( $FAD^{\bullet-}$ ; black), illuminated with a 450-nm laser ( $FADH^{\bullet}$  state; blue) and following exposure to 380-, 450-, and 620 nm LEDs ( $FADH^{\bullet}$  state; red). Incubation at room temperature in the dark overnight leads to return of the  $FAD^{\bullet-}$  state (green). A slight increase in the absorption of  $FAD^{\bullet-}$  is observed due to evaporation over the 24-h period and a small degree of aggregation, leading to scattering at lower wavelengths. (C) Oxidation of the  $FADH^{\bullet}$  state of *C/CRY4* can be monitored at 450 nm (black) and 478 nm (red) ( $FAD^{\bullet-}$  state) or 633 nm ( $FADH^{\bullet}$ ). Oxidation proceeds with the formation of  $FADH^{\bullet}$  ( $\tau = 2,600$  s), the concentration of which remains relatively stable throughout the duration of the experiment (blue). Oxidation to  $FAD^{\bullet-}$  as determined proceeds with a time constant of 4,300 s. See also *SI Appendix, Fig. S1*.

birds (24) and immunohistochemical assays suggest CRY photochemical activation (25).

These results are not without controversy or complication, as discrepancies between the biological and chemical data exist. First, migratory animals do not contain photoactive type I CRYs, but rather only type II and IV CRYs are present (26). Second, despite complementation in T-maze assays and expression in the outer retina of birds, type II CRYs are not known to bind FAD with a biologically relevant affinity and thus are unlikely to function as light-dependent magnetosensors (15). Third, CRY action spectra derived from behavioral studies conflict with known FAD absorption spectra. The action spectra for bird orientation in behavioral assays show clear activity in the blue region of the spectrum, consistent with  $FAD^{\bullet-}$  as the ground state; however, orientation has been observed for light wavelengths of up to  $\sim 565$  nm, where  $FAD^{\bullet-}$  does not absorb (2, 25, 27). Fourth, a report indicated that magnetic field-dependent orientation can only occur when the magnetic field is applied in the dark during successive light-dark cycles (27). These latter 2 factors would be inconsistent with a radical pair mechanism based on M1; rather, they are spectrally and chemically more consistent with an M2-based pathway, in which light drives the conversion of  $FADH^{\bullet}$  to  $FADH^-$  and reoxidation in the dark forms a semiquinone-superoxide  $[FADH^{\bullet} O_2^{\bullet-}]$  radical pair (M2; Fig. 14). We note that such a pathway itself is contradictory, as the extremely fast spin relaxation in superoxide renders M2 unsuitable as a magnetosensor (28).

Inconsistencies between CRY photochemistry and behavioral assays in migratory birds may have been reconciled with recent studies. CRY4 proteins are specific to birds, amphibians, fish, and reptiles; are photochemically active (9, 12); and recently were found to be expressed in the outer segments of double-cone photoreceptor cells and long-wavelength cones of European robins in a seasonal-dependent manner (13); however, their mechanisms of signal transduction are poorly understood. Here we report the structure of a photoactive vertebrate cryptochrome from pigeon that identifies an evolutionarily conserved photochemical pathway that retains the necessary elements to function as a candidate magnetosensor.

## Results

**Photochemical Characterization of a Type IV CRY from Pigeon, *Columba livia* (*C/CRY4*).** Consistent with recently published reports (11), photochemical characterization of both full-length (FL) *C/CRY4* and a construct truncated at the C terminus by 28 residues that contains the photolyase homology region (PHR) demonstrate spectra consistent with bound  $FAD^{\bullet-}$  in the ground state (Fig. 1B and *SI Appendix, Fig. S1A*). On illumination, *C/CRY4* is reduced to the  $FADH^{\bullet}$  state, characterized by bleaching of the 450-nm

band and an increase in a broad absorption from 550 nm to 690 nm ( $\lambda_{\max} = 633$  nm) (Fig. 1B). Further exposure to UV-blue or red light leads to loss of the 550-nm to 690-nm signature and formation of a primary peak centered at 380 nm, consistent with generation of the fully reduced  $FADH^-$  state from  $FADH^{\bullet}$  (29). On return to the dark, *C/CRY4* undergoes slow reoxidation to  $FADH^{\bullet}$  ( $\tau = 2,600$  s) and  $FAD^{\bullet-}$  ( $\tau = 4,300$  s) (Fig. 1C).

These spectral characteristics deviate from other characterized CRYs. First, we observe an  $\sim 40$ -nm red shift in  $FADH^{\bullet}$  (peaks at 591 and 633 nm) compared with *Arabidopsis thaliana* CRY1 (*AtCRY1*) (Fig. 1B and *SI Appendix, Fig. S1A*) (30). These spectral signatures are more similar to photolyases and those observed in the animal-like CRY from *Chlamydomonas reinhardtii*, which functions under red light in vivo (31). Second, photoreduction proceeds in a clear stepwise fashion, with formation of a spectrally defined and long-lived  $FADH^{\bullet}$  state. Such behavior is similar to that of photolyases, where  $FADH^{\bullet}$  is stabilized and formation of  $FADH^-$  is pronounced, but contrasts with that of plant CRYs, where further reduction of  $FADH^{\bullet}$  is limited (32–34). In this manner, *C/CRY4* retains several characteristics of photolyases that deviate from animal and plant CRYs; namely, photochemical reduction proceeds in a stepwise manner to generate relatively stable  $FADH^{\bullet}$  and  $FADH^-$  states.

To further elucidate functional photochemical differences in *C/CRY4*, we examined the kinetics of photoreduction under varying light intensities and spectral profiles to extract the quantum yields of photoreduction (*SI Appendix, Figs. S1–S3*). In brief, *C/CRY4* samples were continuously irradiated (using light-emitting diodes [LEDs]) with either UV-blue light (380 and 450 nm LEDs) or UV-blue supplemented with red light (380, 450, and 620 nm LEDs) at low (LL;  $14 \mu\text{mol m}^{-2} \text{s}^{-1}$ ), medium (ML;  $18 \mu\text{mol m}^{-2} \text{s}^{-1}$ ), or high (HL;  $20 \mu\text{mol m}^{-2} \text{s}^{-1}$ ) intensity or with an intense broad-spectrum source (BSHL;  $142 \mu\text{mol m}^{-2} \text{s}^{-1}$ ). Under all conditions, kinetic profiles demonstrated clear and distinct stepwise photoreduction of  $FAD^{\bullet-}$  to  $FADH^{\bullet}$  and subsequently to  $FADH^-$ . Comparisons of kinetics under the varying spectral profiles indicate that conversion of  $FADH^{\bullet}$  to  $FADH^-$  is enhanced by red light due to the presence of the 40-nm red shift in the broad absorption band of  $FADH^{\bullet}$  (Fig. 2A and B and *SI Appendix, Fig. S1*).

To further characterize the efficiency of photoreduction, we extracted the quantum yields directly from the photoreduction kinetics (*SI Appendix, Figs. S1–S3*). Extraction of the quantum yields for PHR and FL *C/CRY4* revealed unexpectedly high yields of photoreduction (*SI Appendix, Tables S2 and S3*), where conversion of  $FAD^{\bullet-}$  to  $FADH^{\bullet}$  proceeded with quantum yields ( $\phi_1$ ) of  $0.37 \pm 0.037$  for PHL constructs and  $0.43 \pm 0.043$  for FL constructs. These values exceed those observed in other animal and

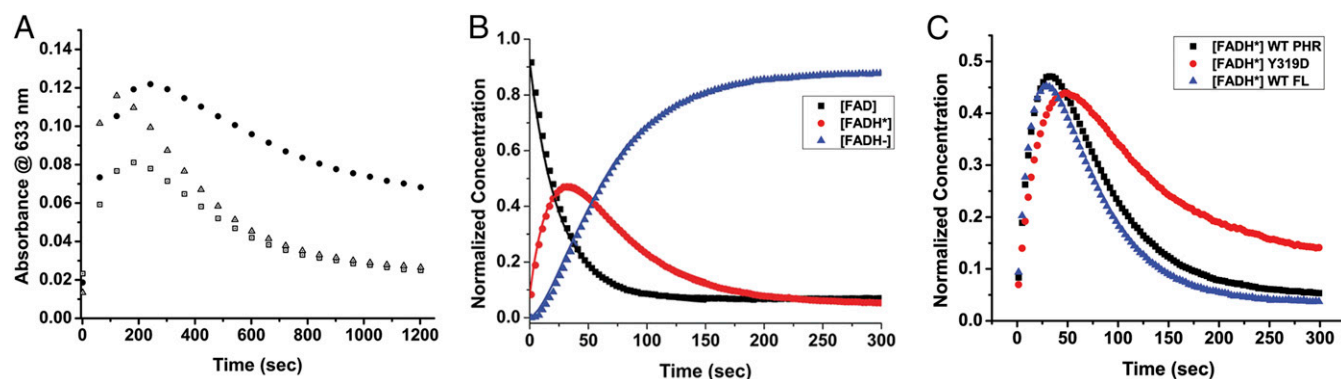


**Fig. 2.** Photoreduction kinetics of *C/CRY4*. (A) Kinetic traces at 633 nm for PHR *C/CRY4* illustrating the formation of  $\text{FADH}^\bullet$  and subsequent conversion to  $\text{FADH}^-$ . In the presence of only 380-nm and 450-nm light, robust conversion to  $\text{FADH}^\bullet$  is observed under LL (solid black circles;  $8 \mu\text{mol m}^{-2} \text{s}^{-1}$ ) or HL (open triangles;  $15 \mu\text{mol m}^{-2} \text{s}^{-1}$ ) light intensities, followed by a slow conversion of  $\text{FADH}^\bullet$  to  $\text{FADH}^-$  that is a function of the light intensity. In the presence of 380-, 450-, and 620-nm light (open squares), the amplitude of the initial formation of  $\text{FADH}^\bullet$  is decreased as it is steadily converted to  $\text{FADH}^-$  throughout the time course. The UV-blue (high) and 380-, 450-, and 620-nm light treatments have the same total photon dose and reach the same steady-state conversion to the  $\text{FADH}^-$  state, indicating that all wavelengths contribute to photoreduction. (B) Normalized concentrations of  $\text{FAD}^{\text{ox}}$  (black),  $\text{FADH}^\bullet$  (red), and  $\text{FADH}^-$  (blue) as a function of time under HL illumination (symbols) and resulting fit to the kinetic model (solid lines) for PHR *C/CRY4*. (C) Comparison of the normalized concentrations of  $\text{FADH}^\bullet$  for PHR (black), Y319D PHR (red), and FL proteins (blue) as a function of time under HL illumination. See also *SI Appendix, Figs. S1–S3*.

plant CRYs, in which typical values for  $\phi_1$  are  $\sim 0.20$  (35, 36). Similarly, quantum yields for conversion of  $\text{FADH}^\bullet$  to  $\text{FADH}^-$  (PHR  $\phi_2 = 0.19$ ; FL  $\phi_2 = 0.23$ ) significantly exceed those observed for other CRYs, where either conversion to  $\text{FADH}^-$  does not proceed (*Drosophila melanogaster*; *DmCRY*) or proceed with quantum yields  $< 0.05$  (*AtCRY1*) (36). Notably, high quantum yields provide sensitivity to low light intensities, as has been observed in behavioral assays of magnetic orientation in birds (2).

***C/CRY4* Crystal Structure Identifies Elements Consistent with Enhanced Formation of Reduced Flavins.** To better understand the molecular origins of the *C/CRY4* photocycle, we determined a high-resolution crystal structure of PHR *C/CRY4*. (*SI Appendix, Table S1* provides crystallographic statistics.) The structure of PHR *C/CRY4* is consistent with the CRY-photolyase family (CPF) (Fig. 3A and *SI Appendix, Fig. S4*) but deviates from all vertebrate structures, in that *C/CRY4* constitutively binds FAD and is photochemically active. *C/CRY4* both resembles and deviates from photoactive type I CRYs in several aspects that impact photochemical behavior. First, *C/CRY4* contains an Asn residue (Asn391) directly adjacent to the N5 position of the FAD isoalloxazine ring (*SI Appendix, Fig. S5A*). The residue identity at this position has been reported to tune FAD photochemistry, where typically type I CRYs, plant CRYs, and photolyases are differentiated by selecting for formation of the  $\text{FAD}^{\bullet-}$  state (type 1: Cys), formation and stabilization of the  $\text{FADH}^\bullet$  state (plant: Asp), or stabilization of  $\text{FADH}^\bullet$  and efficient formation of  $\text{FADH}^-$  (photolyases: Asn) (35, 37). Notably, Cys $\rightarrow$ Asn mutations in type 1 CRYs lead to selection for the  $\text{FADH}^\bullet$  state and increases in  $\phi_1$  from  $\sim 0.17$  to 0.41 (35). Thus, the presence of Asn391 is consistent with photolyase-type chemistry and the observed relative aerobic stability of  $\text{FADH}^\bullet$  in *C/CRY4*.

In addition to modifications within the FAD active site, the *C/CRY4* structure reveals alteration to the Trp-triad chain that has possible consequences for *C/CRY4* function. *C/CRY4* conserves the Trp-triad ( $\text{W}_{\text{A-C}}$ ), including a fourth Trp residue ( $\text{W}_{\text{D}}$ ) identified in *DmCRY* that enhances photoactivity (Fig. 3B) (38, 39). Surprisingly, a possible fifth redox active element unique to CRY4 proteins is also present. Directly adjacent to  $\text{W}_{\text{D}}$  lies a solvent-exposed Tyr (Tyr319;  $\text{Y}_{\text{E}}$ ), only 3.9 Å away from Trp369 ( $\text{W}_{\text{D}}$ ). Tyr319 is anchored in a solvent-filled cleft through a tightly bound water molecule bridging Tyr319, Arg324, and Arg477 (*SI Appendix, Fig. S5B*). Examination of CRY4 protein sequences reveals that Tyr319 is highly conserved in CRY4 proteins but divergent from that in *DmCRY* (Ala339) and type II CRYs

(conserved Asp; Fig. 3C). Terminal Tyr residues in the electron transport chain have been verified to be required for signal transduction in animal-like CRYs, and Tyr radicals demonstrate unusually long lifetimes (31).

Structural and photochemical characterization of a Y319D variant of the PHR construct indicates that introduction of Asp319 does not affect the structure of *C/CRY4* but does result in significant perturbation to its *C/CRY4* photocycle (Fig. 3B and *SI Appendix, Figs. S1 and S6*). Namely, photoreduction of Y319D proceeds with significantly decreased quantum yields ( $\phi_1 = 0.23 \pm 0.023$ ;  $\phi_2 = 0.13 \pm 0.013$ ) and alterations to the reoxidation kinetics (*SI Appendix, Figs. S1 and S5 and Tables S2 and S3*). The evolutionary conservation of Tyr319 in CRY4 proteins, the effect of Y319D variants on quantum yields, and the effect on the kinetics of reoxidation have possible functional consequences for magnetoreception. First, high quantum yields enable photoactivation even under low light intensities where many migratory birds show principal activity in migration (2, 25, 40). Second, the red shift in the  $\text{FADH}^\bullet$  radical compared to *AtCRY* increases the sensitivity of a  $\text{FADH}^\bullet$  signaling state to red light. Third, slow reoxidation kinetics enables accumulation of reduced flavin species even under low light intensities. These results suggest that *C/CRY4* retains the functional photochemical elements necessary to reconcile most discrepancies between CRY photochemistry and behavioral assays in migratory birds. As outlined in the discussion below, 3 behavioral observations remain unexplained.

**Y319D Alters Photochemical Pathways in *C/CRY4*.** Transient absorption measurements of PHR *C/CRY4* and the Y319D variant provide insight into the photochemistry on early timescales. The time-resolved spectra (Fig. 4A and B, respectively) strongly resemble those of *DmCRY* (39). Photoinduced electron transfer occurs on a faster timescale than the spectrometer resolution ( $\sim 100$  ps) to form the anionic semiquinone,  $\text{FAD}^{\bullet-}$ , and a cationic tryptophan radical,  $\text{TrpH}^{\bullet+}$ , whose absorption (550 to 600 nm) decays with a time constant of 500 to 700 ns. The disappearance of this signal is consistent with either deprotonation of  $\text{TrpH}^{\bullet+}$  to form the neutral  $\text{Trp}^\bullet$  radical, as has been observed for type I CRYs and photolyases (17, 41), or electron transfer from Y319 to  $\text{TrpH}^{\bullet+}$  to give a Tyr radical, which is expected to absorb at  $\sim 410$  nm (42). While there is no obvious spectral feature in Fig. 4A that would identify a Tyr radical, we did find a long-lived absorption at 410 nm that was absent for Y319D (Fig. 4C). Assignment of this signal to a persistent Tyr radical would be consistent



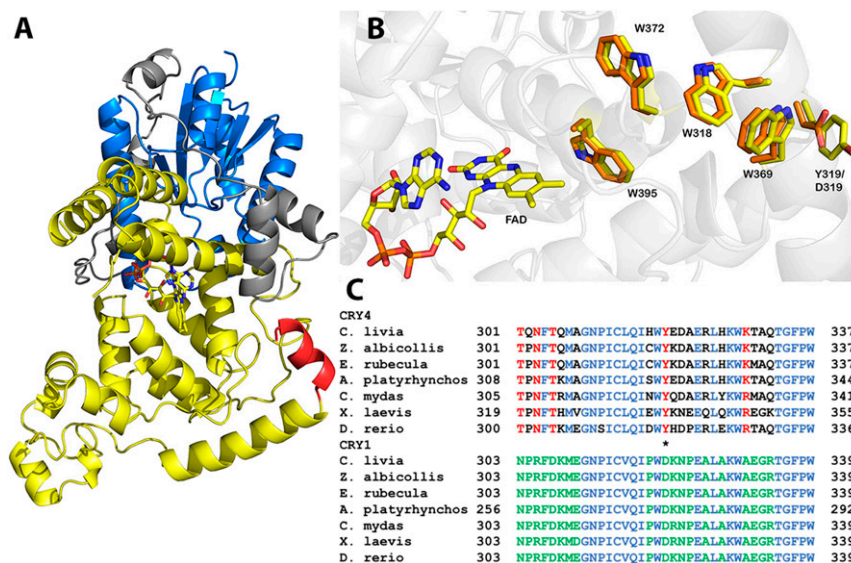


**Fig. 3.** *C/CRY4* structure. (A) Pigeon CRY contains a typical CPF fold consisting of an  $\alpha$ -domain (blue) connected to an all-helical domain (yellow) by a flexible linker (gray). The initial part of the CTT (red) is present and oriented toward the FAD-binding pocket. (B) All 4 Trp residues involved in the *DmCRY* Trp-tetrad are conserved in the WT *C/CRY4* PHR structure (yellow); these include W395 ( $W_A$ ), W372 ( $W_B$ ), W318 ( $W_C$ ), and W369 ( $W_D$ ). An additional possible electron donor, Y319, lies adjacent to W369. Introduction of a Y319D mutation (orange) does not alter the structure of *C/CRY4*. (C) Sequence alignment of CRY4 and CRY1 proteins in representative species. Residues conserved in both CRY1 and CRY4 proteins are shown in blue, residues conserved in CRY1 only are shown in green, and residues conserved in CRY4 proteins are highlighted in red. Tyr319 differentiates CRY4 and CRY1 proteins, where a Tyr is highly conserved in CRY4 proteins, and the residue is replaced with an Asp in CRY1s. See also *SI Appendix, Fig. S4*.

with recently published reports on an animal-like CRY and a photolyase with an altered electron transport pathway (31, 43). It could also account for the larger quantum yields of  $\text{FADH}^+$  and  $\text{FADH}^-$  in *C/CRY4* compared with Y319D. Based on these factors, we tentatively assign the long-lived absorption at 410 nm to a Tyr radical, although alternative mechanisms by which Y319D alters the *C/CRY4* photocycle cannot be ruled out.

**The *C/CRY4* Structure Identifies a Type I-Like Light-Dependent Conformational Change.** Photochemical and structural data of *C/CRY4* and the Y319D variant might reconcile conflicts between CRY photochemistry and behavioral assays; however, they do not shed light on a mechanism whereby photoreduction leads to a conformational change that can induce signaling. A cursory sequence examination of *C/CRY4* demonstrates higher conservation with light-independent type II CRYs (~54% identity) than with photoresponsive type I CRYs (~37% identity); however, examination of the *C/CRY4* structure reveals conserved elements that block type II signaling mechanisms and favor a light-dependent mechanism consistent with a type I-like conformational change.

Topologically, *C/CRY4* demonstrates a structure consistent with the CPF family, where *C/CRY4* can be separated into 3 structural domains, an N-terminal  $\alpha$ -domain connected via a long flexible linker to an all-helical C-terminal domain (Fig. 3A). Directly adjacent to a C-terminal coiled-coil helix is a sharp turn leading into the beginning of the highly divergent C-terminal tail (CTT) (Fig. 3A). Although the entire CTT is not present, the initial residues form a helical element that runs along a groove formed from the C-terminal lid and the long flexible linker and is oriented toward the FAD-binding cleft. Such an orientation is consistent with the CTT docking in a manner analogous to *DmCRY*, where blue light excitation of FAD can lead to conformational changes in the CTT (9, 44).

Examination of the FAD-binding cleft reveals conservation of key amino acids required for DNA repair activity in photolyases and signal transduction in type I CRYs. Namely, adjacent to the adenine moiety of FAD lies a conserved pocket that recognizes an FFW motif in the CTT of *DmCRY* or DNA photolesions in photolyases (Fig. 5). In *C/CRY4*, this pocket is retained, and in the absence of the CTT, a glycerol molecule occupies the active site

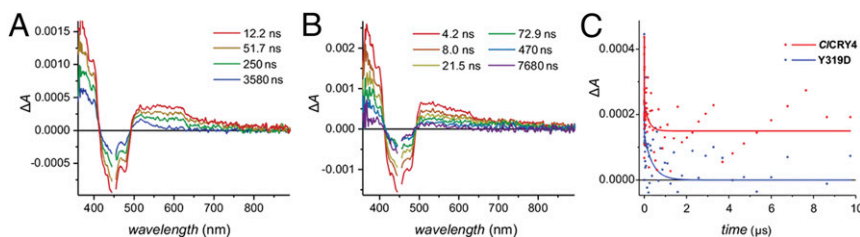


**Fig. 4.** Transient absorption of *C/CRY4* and Y319D. (A) Differential absorption spectra of PHR *C/CRY4* showing the major spectral changes over a 10- $\mu$ s collection window. Protein samples were prepared so that their ground state absorption at 450 nm was between 0.7 and 0.8. Excitation was at 450 nm. The major species contributing at early times are  $\text{FAD}^{+}$  and  $\text{TrpH}^{+}$ , which deprotonates to form  $\text{Trp}^+$  and/or is reduced by electron transfer from Y319. The protonation state of the flavin is unchanged on this timescale. (B) Differential absorption spectra of Y319D showing the same general chemistry as *C/CRY4* but with a greater loss of the radical pair. (C) Comparison of the differential absorption as a function of time at 410 nm reveals a long-lived species that absorbs at this wavelength in *C/CRY4* (red). At the same wavelength, the absorption for Y319D decays completely within the first few microseconds (blue). Points represent the individual times, and the solid lines represent the result of exponential fits to the data with (*C/CRY4*) or without (Y319D) a constant offset.

lined by Trp290/Trp397 and His353/His357 (Fig. 5A). Notably, His353 forms an H-bond to the ribityl side chain of FAD in a manner analogous to *DmCRY*, where changes in protonation of the equivalent His (His378) following photoexcitation leads to release of the CTT (45). Despite conservation of similar elements within the CTT binding groove, there are notable deviations within the phosphate-binding motif (PBM; residues 235 to 245) that interacts with the CTT in *DmCRY*. In *C/CRY4*, no electron density is observed for residues 225 to 246 that compose the PBM responsible for alteration in local structure to accommodate the CTT in *DmCRY* (38, 45, 46). In *DmCRY*, limited proteolysis assays indicate coupling of the CTT and PBM in light-dependent order-disorder transitions, whereupon the PBM becomes more protected in the light state following CTT release (deprotection) (47, 48).

Limited proteolysis assays on *C/CRY4* under light and dark conditions confirm conformational changes in the PBM. For limited proteolysis experiments, sequence numbering includes 5 amino acids that result from cloning artifacts (GAMGS). Comparisons of proteolysis products under light and dark conditions reveal that photoactivation of *C/CRY4* leads to protection from proteolysis (Fig. 5C). Mass spectrometry analysis of the proteolysis products reveals that the primary site of light-induced protection occurs within the PBM and CTT motifs. Namely, 3 proteolysis sites are protected in the light that correspond to fragments 1 to 237, 214 to 530, and 238 to 511, which differ in cleavage of the CTT motif (residues 508 to 530) and cleavage within the PBM. Similar to *DmCRY*, light induces protection of the PBM consistent with a local ordering event; however, in contrast to *DmCRY*, the CTT appears to be mutually protected with the PBM on photoactivation.

These results indicate that photoactivation of *C/CRY4* is coupled to order-disorder transitions as observed in type I CRYs, but they differ in terms of the apparent involvement of the CTT.

**Tyr107 Disrupts a Type II-Like Signaling Mechanism.** Type II CRYs function primarily through modulation of circadian clock transcription via light-independent repression of the circadian clock transcription factors CLOCK and BMAL. CRY-mediated repression is dependent on complexation with CLOCK through interactions involving a secondary pocket of the CRY  $\alpha\beta$ -domain (49, 50). Previous studies of CRY4 proteins from zebrafish indicate that they are unable to rescue type II CRYs in BMAL repression assays (51). Examination of the secondary pocket in *C/CRY4* reveals several differences compared with other animal CRYs. First, the secondary pocket is largely formed by 2 adjacent loops/helices termed the upper and lower helices. Whereas the upper helix is well-folded in all CRY proteins, the lower helix often forms a disordered loop in the absence of recognition partners or pigments (Fig. 5D). In *C/CRY4*, both elements are well folded and sequester a solvent-filled cavity, despite the absence of a cofactor or recognition target. Examination of residues lining the upper and lower helices indicates that Tyr107 juts into the secondary pocket, partially occluding the CLOCK interaction site (Fig. 5D). In this manner, Tyr107 may be responsible for the inability of CRY4 proteins to rescue type II function and may also stabilize the lower helix by restricting movement within the secondary pocket. Indeed, a G106Y mutant that mimics Tyr107 in mouse CRY1 is unable to rescue circadian functionality in complementation assays (*SI Appendix, Fig. S7*). Thus, evolutionary divergence in residues lining the secondary pocket likely disrupts type II CRY signaling in CRY4 proteins.

## Discussion

Even though we are aware that pigeons are not night-migratory songbirds, the sequences of their CRY4 proteins are very similar, including conservation of Y319, and thus in the following discussion, we assume that CRY4 from pigeons and night-migratory songbirds have similar photochemistry. The primary complications in correlating CRY photochemistry to magnetoresponsive signaling are related to discrepancies between CRY photochemistry and behavioral responses—namely, that the behavioral responses are exquisitely sensitive to low-intensity light, and birds seem to be able to orient magnetically under a wide spectrum of light (2, 25, 27, 52). Here we address 3 constraints on a candidate magnetosensor. First, most songbirds migrate at night, when light intensities are  $<1$  lx (1). Under these conditions, population of a  $\text{FADH}^\bullet$  signaling state via M1 alone is minimal in vitro (*SI Appendix, Fig. S8*). Second, behavioral responses in migratory birds have been reported to be affected by green/red light in some experiments. These results contrast with the absorption spectrum of  $\text{FAD}^{\text{ox}}$ . Third, the magnetic field-dependent radical pair must alter the population of a signaling state of the photosensor by being coupled to a defined conformational change resulting from a change in the redox state of the FAD chromophore.

Based on chemical and structural characterization of *C/CRY4*, we have deduced the following. First, photoreduction of *C/CRY4* results in a type I CRY-like conformational change involving order-disorder transitions within the PBM. Notably, the nature of the involvement of the CTT diverges in the type IV CRYs, where an increase in proteolysis is not observed and the CTT rather may be protected in the light. Furthermore, in contrast to recent molecular dynamics simulations of *C/CRY4*, crystal structures of WT and Y319D PHR domains confirm that His353 contacts the ribityl chain of FAD to enable type I-like protonation events to affect contacts to the CTT in the ground and/or signaling states (45, 53). Thus, based on limited proteolysis assays, the primary photochemical events mirror type I CRYs, in which initial formation of the semiquinone state of FAD could propagate to the FAD-binding cleft to alter the protonation state of a conserved His residue.

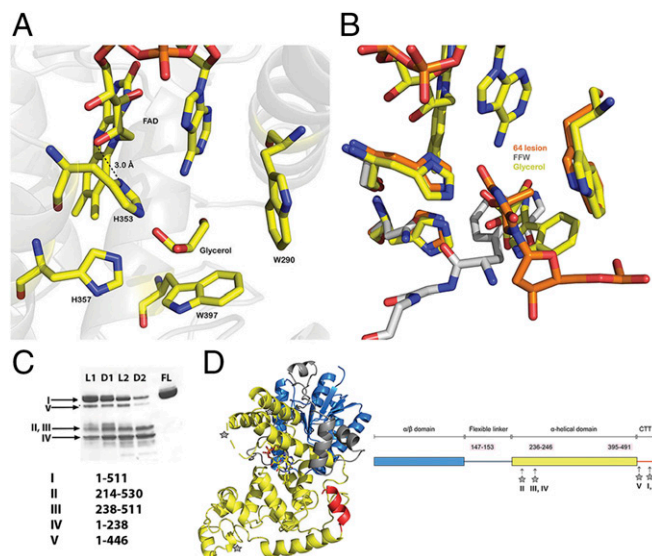


**Fig. 5.** Conservation of a type I signaling mechanism. (A) A glycerol molecule binds to the photoreaction/photosignaling site formed by His353/357, W290/397, and the adenine side chain of FAD. His353 is conserved with *DmCRY* and forms the proximal contact to FAD via an H-bond to a hydroxyl group within the ribose moiety. (B) Comparison of the photoreaction/photosignaling sites of *DmCRY* (gray), *C/CRY4* (yellow), and *Drosophila* 6-4 photolyase (orange). The FFW motif of the *DmCRY* CTT, the 6-4 photolesion, and the glycerol moiety bind to a solvent-exposed cleft anchored by conserved His/Asn and Trp residues. His353 (*C/CRY4*) is structurally equivalent to *DmCRY* His378, which is required for signal transduction. (C) Limited proteolysis assays of FL *C/CRY4* illumination with a broad-spectrum light source for 10 min before proteolysis for either 10 or 30 min (L1 and L2, respectively) results in protection of several degradation bands compared with samples kept in the dark (D1 and D2). Mass spectrometry analysis of the degradation fragments indicates primary protected sites within the PBM and CTT motifs. (D) Schematic and cartoon indicating proteolysis sites. See also *SI Appendix, Figs. S4 and S7*.



Second, evolutionary conservation of Tyr319 and Asn391 imparts high quantum yields of photoreduction, allowing efficient formation of reduced flavin species under low light conditions by extending the Trp-tetrad chain (Tyr319) and stabilizing the FADH<sup>•</sup> state (Asn391). Efficient formation of FADH<sup>•</sup> and FADH<sup>−</sup> are essential for light-dependent function via an M1-based (FADH<sup>•</sup>) or M2-based (FADH<sup>−</sup>) mechanism. Modeling of CRY photochemical dynamics under different lighting conditions confirms that the increased efficiency allows for population of FADH<sup>•</sup> under light intensities consistent with dusk (*SI Appendix, Fig. S8*). In this regard, the high quantum yields of photoreduction support behavioral assays in which light intensities corresponding to dusk conditions are sufficient to drive a behavioral response (40). Furthermore, comparing *CiCRY4* chemistry under peak daylight intensities (108,000 lx), cloudy conditions (1,500 lx), sunset conditions (400 lx), and intense moonlight (0.5 lx) sheds light on possible mechanisms of *CiCRY4* function in magnetosensing (*SI Appendix, Fig. S8*); namely, under peak daylight intensities, *CiCRY4* exists primarily in the FADH<sup>−</sup> state. However, under cloudy conditions, in which magnetic fields have been shown to affect homing pigeon orientation, the FADH<sup>•</sup> state is efficiently populated (54, 55). In contrast, under moonlight conditions, when many migratory songbirds navigate (1), *in vitro* photochemistry indicates that the FADH<sup>•</sup> state represents <1% of the FAD pool. The latter data indicate that direct population of FADH<sup>•</sup> via M1 under moonlight conditions will be limited.

We present 2 possible biological mechanisms that may facilitate CRY function as a magnetosensor under moonlight conditions. First, CRY reoxidation kinetics are oxygen-dependent. Currently, the oxygen tension in magnetoresponsive cells is unknown. A low oxygen content in magnetoresponsive cells would further stabilize FADH<sup>•</sup>, allowing accumulation via M1 even at 0.5 lx. Second, a modified M2 pathway may be present in which the radical pair involves an unknown radical species different from superoxide. Such a mechanism has been proposed elsewhere (56); however, no candidate species currently exist. Under such a mechanism, a pool of signaling-inactive FADH<sup>−</sup> would accumulate during the day through M1. After nightfall, the slow reoxidation kinetics would allow repopulation of the FADH<sup>•</sup> signaling state throughout the night via this M2-like mechanism. This pathway would allow both M1 and M2 to contribute to magnetoresponsive signaling that can persist under nighttime conditions (*SI Appendix, Fig. S8*). It is relevant that each FADH<sup>•</sup> species accumulated during the day can be used to produce FADH<sup>•</sup> only once per night, whereas the M1 mechanism can be recycled by subsequent photon absorptions. The resulting model can reconcile possible conflicts with generating a signaling state under low-light conditions and conflicts with a solely M2-based mechanism, which is unlikely due to the fast spin relaxation of superoxide.

Any mechanism suggesting that a magnetic field-dependent signal could be generated during the day and then used at night is at odds with behavioral data. In a free-flight experiment, birds that had sensed a rotated field during the sunset period calibrated their magnetic flight directions from the setting sun and reoriented to the natural field in less than 5 min (57). Furthermore, the numerous experiments in which birds are placed for 1 h in Emlen funnel cages under moonlight conditions and orient in accordance with a horizontally rotated magnetic field after being held in the natural magnetic field during the day exclude the possibility that magnetic information accumulated during the day is used during the subsequent night (58, 59). These results indicate that light must be present contemporaneously with generation of the magnetic field-sensitive radical pair, thereby excluding a light-independent M2 mechanism based on reoxidation of previously formed FADH<sup>−</sup>. An alternative light-dependent M2 mechanism could exist that mirrors a photolyase mechanism (photolyase-like M2), in which photon absorption leads to highly efficient electron transfer to a DNA lesion. For magnetoresponsive

CRYs, such a mechanism would require an electron acceptor with suitable spin dynamics. Currently, no such acceptor is known; however, the DNA-binding site is exposed in *CiCRY4* and is poised to interact with small molecules or protein targets.

Essential to both M1 and a light-dependent photolyase-like M2-based mechanism are 2 features conserved in *CiCRY4*. First, an efficient population of reduced flavin species under low light conditions is essential. Second, for a light-dependent M2-based mechanism, the FADH<sup>−</sup> state must be stabilized so as to disallow competing formation of FADH<sup>•</sup> via light-independent mechanisms. It is possible that CRYs use both pathways depending on environmental conditions and migratory time of day.

We note that the foregoing mechanisms are still unable to resolve 3 conflicts within the magnetosensor literature, but keep in mind that purified CRY4 *in vitro* could be less sensitive than CRY4 in its natural surroundings in a magnetoreceptor cell. Previous behavioral studies have suggested that green light is capable of affecting orientation behavior (2, 40). For an FAD (M1) or FADH<sup>−</sup> (M2) ground state, green light would not be able to initiate a photochemical response and thus is inconsistent with *in vitro* CRY photochemistry. Similarly, results of behavioral experiments in fruit flies are inconsistent with known FAD chemistry, with T-maze assay results showing that light >420 nm is incapable of generating a response (22). Two possible scenarios have been proposed to reconcile the observed results. In fruit flies, CRYs could bind an antennae cofactor that contributes to FAD activation. Antennae pigments in photolyases absorb in the UV region (60). However, such a scenario is unlikely, as structural studies of *CiCRY4* and *DmCRY* indicate that the antenna-binding pocket is occluded by Tyr107 (*CiCRY4*) or Trp114 (*DmCRY*), disrupting the ability to bind pigments in this pocket (44), and no alternative antenna-binding sites have been identified in these proteins. Alternatively, it has been suggested that other visual photoreceptors may contribute to the signaling response. This could reconcile the observed behavioral data but remains unverified experimentally. The remaining factor that conflicts with a CRY-based model is the observed orientation behavior when magnetic fields are applied only in the dark in successive light-dark cycles (27). In such experiments, the dark phase occurs within a 700-ms timeframe. Given the slow reoxidation pathways present in *CiCRY4*, almost no signal could be generated via M2 even if M2 were viable in magnetosensing. Thus, such a pathway as a signaling mechanism remains unlikely. New behavioral studies could help resolve these unanswered questions. Furthermore, future photochemical studies in migratory birds may improve our understanding of organism-specific biological adaptation.

## Materials and Methods

**Protein Expression and Purification.** Pigeon *Cry4* cDNA was synthesized based on published reports (61). *CiCRY4* PHR (residues 1 to 497) and *CiCRY4* FL (residues 1 to 525) DNA fragments were cloned into pFastBac HTb vector using BamHI/XhoI sites.

Protein was expressed in sf9 cells in the dark. Frozen cell pellets were lysed by sonication in a lysis buffer containing 20 mM Tris pH 7.5, 300 mM NaCl, 5% glycerol, 2.5 mM CHAPS, and protease inhibitors (Pierce, catalog no. A32965). Clarified cell lysate was applied to a Ni-NTA agarose column (Qiagen; catalog no. 1018244) equilibrated with lysis buffer, and the bound protein was eluted with 50 mM Tris pH 7.8, 300 mM NaCl, 5% glycerol, and 400 mM imidazole. The pooled fractions were buffer-exchanged into 20 mM Hepes pH 7.5, 150 mM NaCl, 5% glycerol, and 2 mM DTT. The His-tag was removed by treatment with TEV protease overnight at 4 °C.

Protein was further purified on an ion-exchange column with a gradient buffer of 600 mM NaCl. As a final purification step, protein was applied to a Superdex 200 size-exclusion column equilibrated in 20 mM Hepes pH 7.5, 150 mM NaCl, 5% glycerol, and 2 mM DTT. All expression and purification steps were performed in dim red light.

**Crystallization and Structure Determination.** PHR *CiCRY4* and Y319D were crystallized using the hanging drop method. Crystals were obtained at 21 °C in dark from a 1:1 mixture of protein (10 to 12 mg/mL) and a reservoir solution

consisting of 5% PEG 6000 and 0.1 M HEPES pH 7.1. For Y319D protein, crystals were obtained using a reservoir solution containing 7.5% PEG 6000 and 0.1 M HEPES pH 7.1. Crystal reached maximum size after 4 to 5 d and were harvested in the dark at that time. Crystals were transferred to cryoprotectant solution consisting of 5% PEG 6000, 0.1 M HEPES pH 7, 2 mM DTT, and either 30% P400 or 30% glycerol and then flash-frozen in liquid nitrogen in the dark.

Diffraction data were collected at the Advanced Photon Source 24-ID-C Northeastern Collaborative Access Team (NE-CAT) beamline for PHR C/CRY4 and at the Advanced Light Source beamline 8.2.1 for Y319D. All data were collected at 100 K. Data were scaled and reduced in HKL2000 (62), and the initial WT structures were obtained using molecular replacement in PHASER (63) with mCRY1 (Protein Data Bank [PDB] ID code 4K0R) as a search model. The initial Y319D structure was obtained by molecular replacement using the WT C/CRY4 as a search model. The final structures were obtained via iterative rebuild cycles in Coot (64) and refinement with PHENIX (65). Atomic coordinates for the reported crystal structures have been deposited in the PDB (ID codes 6PU0 and 6PTZ).

**Mutagenesis.** Mutagenesis of C/CRY4 was performed using a protocol described elsewhere (66). The following primers were used in mutagenesis studies:

Y319D: forward, 5'-CCA ATC TGT CTG CAG ATC CAC TGG GAC GAA GAT GCA GAA AGA CTG; reverse, 5'-GAT CTG CAG ACA GAT TGG ATT CCC TGC CAT CTG TGT GAA.

**Proteolysis.** For light-state experiments, 10  $\mu$ g of FL C/CRY4 was exposed to light for 10 min before proteolysis, and for dark-state experiments, the protein was kept in the dark. Trypsin from bovine pancreas (Sigma-Aldrich) was diluted in 20 mM HEPES pH 7.5 and 300 mM NaCl and then added to protein at 1:100, 1:200, and 1:300 (wt/wt) for 30 min at room temperature. For chymotrypsin experiments, varying amounts were added (0.1, 0.2, and 0.4  $\mu$ g) for 10- and 30-min digestions.

**Mass Spectrometry.** Protein gel pieces were reduced and alkylated with DTT (20 mM) and iodoacetamide (27.5 mM). A 0.01  $\mu$ g/ $\mu$ L solution of trypsin in 50 mM triethylammonium bicarbonate (TEAB) was added to completely cover the gel, which was allowed to sit on ice, after which 50  $\mu$ L of 50 mM TEAB was added, and the gel pieces were digested overnight (Pierce). Following solid-phase extraction cleanup with an Oasis HLB 96-well plate (30  $\mu$ m; Waters), the resulting peptides were dried and then reconstituted in 2% (vol/vol) acetonitrile (ACN) and 0.1% trifluoroacetic acid in water. Samples were injected onto an Orbitrap Fusion Lumos mass spectrometer (Thermo Fisher Scientific) coupled to an Ultimate 3000 RSLC-Nano liquid chromatography system (Dionex). Samples were injected onto a 75- $\mu$ m-i.d., 50-cm long EasySpray column (Thermo Fisher Scientific) and then eluted with a gradient from 1% to 28% buffer B over 60 min. Buffer A contained 2% (vol/vol) ACN and 0.1% formic acid in water, and buffer B contained 80% (vol/vol) ACN, 10% (vol/vol) trifluoroethanol, and 0.1% formic acid in water. The mass spectrometer was operated in positive ion mode with a source voltage of 2.0 kV and an ion transfer tube temperature of 275  $^{\circ}$ C. MS scans were acquired at 120,000 resolution in the Orbitrap, and up to 10 MS/MS spectra were obtained in the Orbitrap for each full spectrum acquired using higher-energy collisional dissociation for ions with charges 2 to 7. Dynamic exclusion was set for 25 s after an ion was selected for fragmentation.

Raw MS data files were analyzed using Proteome Discoverer v2.2 (Thermo Fisher Scientific), and peptide identification was performed using Sequest HT. Fragment and precursor tolerances of 10 ppm and 0.6 Da were specified, with carbamidomethylation of Cys set as a fixed modification and oxidation of Met set as a variable modification. A tryptic peptide search with 3 missed cleavages was performed to identify peptides in all samples, as was a non-specific search to identify N-terminal and C-terminal peptides from the chymotrypsin-limited proteolysis samples.

**UV-Vis Spectroscopy and Kinetics.** For spectroscopic and kinetic measurements, C/CRY4 samples were diluted to 30 to 40  $\mu$ M in buffer containing 20 mM HEPES pH 7.5, 300 mM NaCl, 5% glycerol, and 2 mM DTT. Protein concentration was verified using the extinction coefficient of the FAD chromophore at 448 nm (11,300 M $^{-1}$  cm $^{-1}$ ) before data collection. All spectroscopic and kinetic measurements were conducted at 297 K on an Agilent 8453 UV-vis spectrophotometer.

For kinetic measurements, samples were continuously illuminated by a Heliospectra RX30 programmable LED lighting system oriented perpendicular to the spectra acquisition path. Six illumination protocols were generated by varying the power supplied to 380-, 450-, and 620 nm LEDs to control both the spectral profile and flux. These included UV-blue conditions using

the 380- and 450-nm LEDs under both LL (8  $\mu$ mol m $^{-2}$  s $^{-1}$ ) and HL (15  $\mu$ mol m $^{-2}$  s $^{-1}$ ) intensities. For quantum yield and kinetics measurements, UV-blue light was supplemented with red light using 380-, 450-, and 620-nm LEDs under LL (14  $\mu$ mol m $^{-2}$  s $^{-1}$ ), ML (18  $\mu$ mol m $^{-2}$  s $^{-1}$ ), or HL (20  $\mu$ mol m $^{-2}$  s $^{-1}$ ) intensities or with an intense broad-spectrum source (BSHL; 142  $\mu$ mol m $^{-2}$  s $^{-1}$ ). Light intensities were measured simultaneously during all data collection using an Ocean Optics Flame-S light meter positioned adjacent to the sample collection position and at the same sample height. This setup allowed simultaneous monitoring of C/CRY4 kinetics with measurement of light intensity during all kinetic runs. Illumination profiles for quantum yield and kinetic acquisition are available in *SI Appendix*, Fig. S2.

For forward kinetic measurements, full spectra were recorded on the Agilent 8453 UV-vis spectrophotometer at time intervals designed to minimize incidental excitation by the probe source. The intervals between spectral acquisitions for the various illumination protocols and samples are provided in *SI Appendix*, Table S4. For extraction of rate constants, the absorbances at 450, 478, and 633 nm were extracted from the resulting spectra and corrected for baseline drift by subtracting the absorbance value at 800 nm.

For reoxidation kinetics, spectra were recorded at 60-s intervals, and rate constants for reoxidation were determined from monoexponential fits for the traces at 450 and 478 nm for return to FAD $^{ox}$  and at 633 nm for oxidation to FADH $^{+}$ . For FADH $^{+}$ , the data were truncated after the peak in the 633-nm trace to provide an estimate of the oxidation kinetics of FADH $^{-}$  to FADH $^{+}$ . We note that the oxidation pathways for flavoproteins are complex and oxygen-sensitive (67), and thus these values represent only estimated relative rates of reoxidation for WT and Y319D under equivalent conditions.

Representative spectra for the 3 FAD redox states of C/CRY4 depicted in *SI Appendix*, Fig. S1A were extracted from kinetic data using the Globe Toolbox as described elsewhere (68, 69). Quantum yields were then extracted from the kinetic data using 2 independent methods. Since the spectral profile and intensity of the excitation source were determined at all kinetic time points, the quantum yield can be directly calculated using the following equation:

$$\phi_i = \frac{k_i}{\int F(\lambda)\sigma(\lambda)d\lambda} \quad [1]$$

where  $F(\lambda)$  represents the measured intensity of the excitation source collected during data acquisition and  $\sigma(\lambda)$  is the absorption cross-section extracted from *SI Appendix*, Fig. S3A.

To avoid any possible systematic errors, the quantum yields of photoreduction were also calculated as described elsewhere (36). In brief, a plot of the observed photochemical rate constants as a function of overlap integral yields a slope equivalent to the quantum yield (*SI Appendix*, Fig. S4). The resulting values from the application of both methods are summarized in *SI Appendix*, Tables S2 and S3. A detailed kinetic model that describes CRY photochemistry and resulting methods for extracting the concentrations of individual species is available in *SI Appendix*.

**Transient Absorbance.** Transient absorption measurements were performed at 278 K on a commercially available spectrometer (Ultrafast Systems EOS) modified for measurements on protein samples. The sample was placed in a quartz cuvette with a 10-mm path length, and temperature control was provided by a cryostat (Oxford Instruments). Excitation was at 450 nm using a mode-locked picosecond Nd:YAG laser and optical parametric generation (OPG) (Ekspla PL2210) with a pulse width of 30 ps and a pump energy of 200  $\mu$ J at 355 nm and OPG (Ekspla PG403). The repetition rate of the spectrometer was 1 kHz. To minimize photodamage, data were collected in short photolysis periods (15 s), followed by delays of 3 to 5 min. Buffer conditions for TA measurements were modified by the addition of 20% glycerol and 3 mM potassium ferricyanide to stabilize the sample and speed up recovery times in the excitation volume. Thus, the final buffer for TA studies contained 20 mM HEPES pH 7.5, 300 mM NaCl, 2 mM DTT, 3 mM K $_4$ [Fe(CN) $_6$ ], and 20% vol/vol glycerol. The total photolysis time during which data were collected was 30 min.

**Experimental Model and Subject Details.** Cry1 $^{-/-}$ /Cry2 $^{-/-}$  mouse embryonic fibroblasts were generated by Andrew Liu and Hiroki Ueda and were gifted to us. The cell line was grown in DMEM containing 10% FBS and 1 $\times$  Pen/Strep antibiotics at 37  $^{\circ}$ C under 5% CO $_2$ . LumiCycle (Actimetrics) recording medium was prepared from powdered DMEM without phenol red containing 4.5 g/L glucose and supplemented with 10 mM HEPES pH 7.20, 100  $\mu$ M luciferin, 1 mM sodium pyruvate, 0.035% sodium bicarbonate, 2% FBS, 1 $\times$  Pen/Strep antibiotics, and 2 mM L-glutamine. LumiCycle recordings were performed at 37  $^{\circ}$ C.

**Real-Time Bioluminescence Rescue Assays.** Rescue assays were performed based on previous protocols (50). A total of  $4 \times 10^5$  *Cry1<sup>-/-</sup>/Cry2<sup>-/-</sup>* mouse embryonic fibroblasts were plated in 35-mm tissue culture dishes and transfected the same day with 4  $\mu$ g of a luciferase reporter [pGL3-P(Per2)-Luc] and 150 ng of a cryptochrome rescue vector [pMU2-P(Cry1)-(intron336)-Cry-Myc, modified with a C-terminal MYC tag] using FuGENE 6 (Promega) according to the manufacturer's instructions. At 72 h after transfection, the cells were synchronized by exchanging the growth medium for growth medium supplemented with 0.1  $\mu$ M dexamethasone and then were returned to the incubator for 2 h. The medium was then replaced by LumiCycle recording medium, and the plates were sealed with vacuum grease and cover glass and transferred to the LumiCycle. Bioluminescence monitoring was performed using a LumiCycle to record from each dish continuously for 70 s every 10 min using a photomultiplier tube at 37 °C. Rescue results were processed using the LumiCycle Analysis software package. The first 24 h of recording was discarded.

**ACKNOWLEDGMENTS.** We thank the beamline staff of the Advanced Light Source at the University of California at Berkeley for help with data collection. This work was funded by the NSF (MCB-1613643, to B.D.Z.), NIH (NS095899 and DA042072, to R.E.H.; R01 GM090247, R01 GM112991, and

R35 GM127122, to C.B.G.), Deutsche Forschungsgemeinschaft (SFB 1372, "Magnetoreception and Navigation in Vertebrates" and GRK 1885, to H.M.), the Air Force Office of Scientific Research (Air Force Materiel Command, USAF Award FA9550-14-1-0095, to P.J.H. and H.M.), the European Research Council (under the European Union's 7th Framework Programme, FP7/2007-2013/ERC Grant Agreement 340451, to P.J.H. and under the Horizon 2020 research and innovation program, ERC Synergy Grant Agreement 810002, to P.J.H. and H.M.). X-ray diffraction experiments on WT protein were performed at the Northeastern Collaborative Access Team beamlines, which are funded by the NIH, National Institute of General Medical Sciences (P30 GM124165). The Pilatus 6M detector on the 24-ID-C beamline is funded by NIH Office of Research Infrastructure Programs High-End Instrumentation Grant S10 RR029205. This research used resources of the Advanced Photon Source, a US Department of Energy (DOE) Office of Science User Facility operated for the DOE Office of Science by Argonne National Laboratory under Contract DE-AC02-06CH11357. The Berkeley Center for Structural Biology is supported in part by the NIH, National Institute of General Medical Sciences, and the HHMI. X-ray diffraction experiments on Y319D mutant protein were conducted on the 8.2.1 (HHMI) beamline at the Advanced Light Source. The Advanced Light Source is supported by the Director, Office of Science, Office of Basic Energy Sciences of the US Department of Energy under Contract DE-AC02-05CH11231. J.S.T. is an HHMI Investigator.

- H. Mouritsen, P. J. Hore, The magnetic retina: Light-dependent and trigeminal magnetoreception in migratory birds. *Curr. Opin. Neurobiol.* **22**, 343–352 (2012).
- R. Wiltschko, D. Gehring, S. Denzau, C. Niebner, W. Wiltschko, Magnetoreception in birds: II. Behavioural experiments concerning the cryptochrome cycle. *J. Exp. Biol.* **217**, 4225–4228 (2014).
- H. Mouritsen, Long-distance navigation and magnetoreception in migratory animals. *Nature* **558**, 50–59 (2018).
- K. Schulten, C. E. Swenberg, A. Weller, A biomagnetic sensory mechanism based on magnetic field modulated coherent electron spin motion. *Z. Phys. Chem.* **111**, 1–5 (1978).
- P. J. Hore, H. Mouritsen, The radical-pair mechanism of magnetoreception. *Annu. Rev. Biophys.* **45**, 299–344 (2016).
- I. A. Solov'yov, K. Schulten, Reaction kinetics and mechanism of magnetic field effects in cryptochrome. *J. Phys. Chem. B* **116**, 1089–1099 (2012).
- S. Worster, D. R. Kattinig, P. J. Hore, Spin relaxation of radicals in cryptochrome and its role in avian magnetoreception. *J. Chem. Phys.* **145**, 035104 (2016).
- A. K. Michael, J. L. Fribourgh, R. N. Van Gelder, C. L. Partch, Animal cryptochromes: Divergent roles in light perception, circadian timekeeping and beyond. *Photochem. Photobiol.* **93**, 128–140 (2017).
- N. Oztürk *et al.*, Comparative photochemistry of animal type 1 and type 4 cryptochromes. *Biochemistry* **48**, 8585–8593 (2009).
- B. D. Zoltowski, K. H. Gardner, Tripping the light fantastic: Blue-light photoreceptors as examples of environmentally modulated protein-protein interactions. *Biochemistry* **50**, 4–16 (2011).
- X. Wang *et al.*, Comparative properties and functions of type 2 and type 4 pigeon cryptochromes. *Cell. Mol. Life Sci.* **75**, 4629–4641 (2018).
- R. Watari *et al.*, Light-dependent structural change of chicken retinal Cryptochrome4. *J. Biol. Chem.* **287**, 42634–42641 (2012).
- A. Gunther *et al.*, Double-cone localization and seasonal expression pattern suggest a role in magnetoreception for European Robin Cryptochrome 4. *Curr. Biol.* **28**, 211–223.e4 (2018).
- S. Worster, H. Mouritsen, P. J. Hore, A light-dependent magnetoreception mechanism insensitive to light intensity and polarization. *J. R. Soc. Interface* **14**, 20170405 (2017).
- R. J. Kutta, N. Archipowa, L. O. Johannissen, A. R. Jones, N. S. Scrutton, Vertebrate cryptochromes are vestigial flavoproteins. *Sci. Rep.* **7**, 44906 (2017).
- B. D. Zoltowski, Resolving cryptic aspects of cryptochrome signaling. *Proc. Natl. Acad. Sci. U.S.A.* **112**, 8811–8812 (2015).
- K. Maeda *et al.*, Magnetically sensitive light-induced reactions in cryptochrome are consistent with its proposed role as a magnetoreceptor. *Proc. Natl. Acad. Sci. U.S.A.* **109**, 4774–4779 (2012).
- T. Yoshii, M. Ahmad, C. Helfrich-Förster, Cryptochrome mediates light-dependent magnetosensitivity of *Drosophila*'s circadian clock. *PLoS Biol.* **7**, e1000086 (2009).
- G. Fedele *et al.*, Genetic analysis of circadian responses to low frequency electromagnetic fields in *Drosophila melanogaster*. *PLoS Genet.* **10**, e1004804 (2014).
- C. N. Giachello, N. S. Scrutton, A. R. Jones, R. A. Baines, Magnetic fields modulate blue-light-dependent regulation of neuronal firing by cryptochrome. *J. Neurosci.* **36**, 10742–10749 (2016).
- R. J. Gegear, A. Casselman, S. Waddell, S. M. Reppert, Cryptochrome mediates light-dependent magnetosensitivity in *Drosophila*. *Nature* **454**, 1014–1018 (2008).
- R. J. Gegear, L. E. Foley, A. Casselman, S. M. Reppert, Animal cryptochromes mediate magnetoreception by an unconventional photochemical mechanism. *Nature* **463**, 804–807 (2010).
- P. A. Guerra, R. J. Gegear, S. M. Reppert, A magnetic compass aids monarch butterfly migration. *Nat. Commun.* **5**, 4164 (2014).
- P. Bolte *et al.*, Localisation of the putative magnetoreceptive protein cryptochrome 1b in the retinae of migratory birds and homing pigeons. *PLoS One* **11**, e0147819 (2016).
- C. Niebner *et al.*, Magnetoreception: Activated cryptochrome 1a concurs with magnetic orientation in birds. *J. R. Soc. Interface* **10**, 20130638 (2013).
- M. Liedvogel, H. Mouritsen, Cryptochromes—a potential magnetoreceptor: What do we know and what do we want to know? *J. R. Soc. Interface* **7** (suppl. 2), S147–S162 (2010).
- R. Wiltschko, M. Ahmad, C. Niebner, D. Gehring, W. Wiltschko, Light-dependent magnetoreception in birds: The crucial step occurs in the dark. *J. R. Soc. Interface* **13**, 20151010 (2016).
- H. J. Hogben, O. Efimova, N. Wagner-Rundell, C. R. Timmel, P. J. Hore, Possible involvement of superoxide and dioxygen with cryptochrome in avian magnetoreception: Origin of Zeeman resonances observed by *in vivo* EPR spectroscopy. *Chem. Phys. Lett.* **480**, 118–122 (2009).
- V. Massey, G. Palmer, On the existence of spectrally distinct classes of flavoprotein semiquinones. A new method for the quantitative production of flavoprotein semiquinones. *Biochemistry* **5**, 3181–3189 (1966).
- T. Kottke, A. Batschauer, M. Ahmad, J. Heberle, Blue-light-induced changes in Arabidopsis cryptochrome 1 probed by FTIR difference spectroscopy. *Biochemistry* **45**, 2472–2479 (2006).
- S. Oldemeyer *et al.*, Essential role of an unusually long-lived tyrosyl radical in the response to red light of the animal-like cryptochrome aCRY. *J. Biol. Chem.* **291**, 14062–14071 (2016).
- R. Banerjee *et al.*, The signaling state of Arabidopsis cryptochrome 2 contains flavin semiquinone. *J. Biol. Chem.* **282**, 14916–14922 (2007).
- A. Berndt *et al.*, A novel photoreaction mechanism for the circadian blue light photoreceptor *Drosophila* cryptochrome. *J. Biol. Chem.* **282**, 13011–13021 (2007).
- J. P. Bouly *et al.*, Cryptochrome blue light photoreceptors are activated through interconversion of flavin redox states. *J. Biol. Chem.* **282**, 9383–9391 (2007).
- N. Oztürk, S. H. Song, C. P. Selby, A. Sancar, Animal type 1 cryptochromes. Analysis of the redox state of the flavin cofactor by site-directed mutagenesis. *J. Biol. Chem.* **283**, 3256–3263 (2008).
- M. Procopio *et al.*, Kinetic modeling of the Arabidopsis cryptochrome photocycle: FAD(0) accumulation correlates with biological activity. *Front. Plant Sci.* **7**, 888 (2016).
- M. J. Damiani, J. J. Nostedt, M. A. O'Neill, Impact of the N5-proximal Asn on the thermodynamic and kinetic stability of the semiquinone radical in photolyase. *J. Biol. Chem.* **286**, 4382–4391 (2011).
- C. Lin, D. Top, C. C. Manahan, M. W. Young, B. R. Crane, Circadian clock activity of cryptochrome relies on tryptophan-mediated photoreduction. *Proc. Natl. Acad. Sci. U.S.A.* **115**, 3822–3827 (2018).
- D. Nohr *et al.*, Extended electron-transfer in animal cryptochromes mediated by a tetrad of aromatic amino acids. *Biophys. J.* **111**, 301–311 (2016).
- R. Wiltschko, K. Stapput, P. Thalau, W. Wiltschko, Directional orientation of birds by the magnetic field under different light conditions. *J. R. Soc. Interface* **7** (suppl. 2), S163–S177 (2010).
- C. Aubert, M. H. Vos, P. Mathis, A. P. Eker, K. Brettel, Intraprotein radical transfer during photoactivation of DNA photolyase. *Nature* **405**, 586–590 (2000).
- B. Giovani, M. Byrdin, M. Ahmad, K. Brettel, Light-induced electron transfer in a cryptochrome blue-light photoreceptor. *Nat. Struct. Biol.* **10**, 489–490 (2003).
- P. Müller, E. Ignatz, S. Kiontke, K. Brettel, L. O. Essen, Sub-nanosecond tryptophan radical deprotonation mediated by a protein-bound water cluster in class II DNA photolyases. *Chem. Sci.* **9**, 1200–1212 (2017).
- B. D. Zoltowski *et al.*, Structure of full-length *Drosophila* cryptochrome. *Nature* **480**, 396–399 (2011).
- A. Ganguly *et al.*, Changes in active site histidine hydrogen bonding trigger cryptochrome activation. *Proc. Natl. Acad. Sci. U.S.A.* **113**, 10073–10078 (2016).
- C. Levy *et al.*, Updated structure of *Drosophila* cryptochrome. *Nature* **495**, E3–E4 (2013).
- N. Oztürk, C. P. Selby, D. Zhong, A. Sancar, Mechanism of photoreception by *Drosophila* cryptochrome: Role of the redox status of the flavin chromophore. *J. Biol. Chem.* **289**, 4634–4642 (2014).
- A. T. Vaidya *et al.*, Flavin reduction activates *Drosophila* cryptochrome. *Proc. Natl. Acad. Sci. U.S.A.* **110**, 20455–20460 (2013).



49. A. K. Michael *et al.*, Formation of a repressive complex in the mammalian circadian clock is mediated by the secondary pocket of CRY1. *Proc. Natl. Acad. Sci. U.S.A.* **114**, 1560–1565 (2017).
50. C. Rosensweig *et al.*, An evolutionary hotspot defines functional differences between CRYPTOCHROMES. *Nat. Commun.* **9**, 1138 (2018).
51. T. Ishikawa, J. Hirayama, Y. Kobayashi, T. Todo, Zebrafish CRY represses transcription mediated by CLOCK-BMAL heterodimer without inhibiting its binding to DNA. *Genes Cells* **7**, 1073–1086 (2002).
52. R. Wiltschko *et al.*, Orientation of migratory birds under ultraviolet light. *J. Comp. Physiol. A Neuroethol. Sens. Neural Behav. Physiol.* **200**, 399–407 (2014).
53. D. R. Kattnig, C. Nielsen, I. A. Solov'yov, Molecular dynamics simulations disclose early stages of the photo-activation of cryptochrome 4. *New J. Phys.* **20**, 083018 (2018).
54. T. E. Dennis, M. J. Rayner, M. M. Walker, Evidence that pigeons orient to geomagnetic intensity during homing. *Proc. Biol. Sci.* **274**, 1153–1158 (2007).
55. C. Walcott, R. P. Green, Orientation of homing pigeons altered by a change in the direction of an applied magnetic field. *Science* **184**, 180–182 (1974).
56. A. A. Lee *et al.*, Alternative radical pairs for cryptochrome-based magnetoreception. *J. R. Soc. Interface* **11**, 20131063 (2014).
57. W. W. Cochran, H. Mouritsen, M. Wikelski, Migrating songbirds recalibrate their magnetic compass daily from twilight cues. *Science* **304**, 405–408 (2004).
58. S. Engels *et al.*, Anthropogenic electromagnetic noise disrupts magnetic compass orientation in a migratory bird. *Nature* **509**, 353–356 (2014).
59. C. M. Hein *et al.*, Night-migratory garden warblers can orient with their magnetic compass using the left, the right or both eyes. *J. R. Soc. Interface* **7** (suppl. 2), S227–S233 (2010).
60. S. Kiontke, P. Gnau, R. Haselsberger, A. Batschauer, L. O. Essen, Structural and evolutionary aspects of antenna chromophore usage by class II photolyases. *J. Biol. Chem.* **289**, 19659–19669 (2014).
61. S. Qin *et al.*, A magnetic protein biocompass. *Nat. Mater.* **15**, 217–226 (2016).
62. A. Otwinowski, W. Minor, Processing of X-ray diffraction data in oscillation mode. *Methods Enzymol.* **276**, 307–325 (1997).
63. A. J. McCoy *et al.*, Phaser crystallographic software. *J. Appl. Crystallogr.* **40**, 658–674 (2007).
64. P. Emsley, K. Cowtan, Coot: Model-building tools for molecular graphics. *Acta Crystallogr. D Biol. Crystallogr.* **60**, 2126–2132 (2004).
65. P. D. Adams *et al.*, PHENIX: A comprehensive Python-based system for macromolecular structure solution. *Acta Crystallogr. D Biol. Crystallogr.* **66**, 213–221 (2010).
66. H. Liu, J. H. Naismith, An efficient one-step site-directed deletion, insertion, single and multiple-site plasmid mutagenesis protocol. *BMC Biotechnol.* **8**, 91 (2008).
67. V. Massey, Activation of molecular oxygen by flavins and flavoproteins. *J. Biol. Chem.* **269**, 22459–22462 (1994).
68. L. J. van Wilderen, C. N. Lincoln, J. J. van Thor, Modelling multi-pulse population dynamics from ultrafast spectroscopy. *PLoS One* **6**, e17373 (2011).
69. L. J. van Wilderen, G. Silkstone, M. Mason, J. J. van Thor, M. T. Wilson, Kinetic studies on the oxidation of semiquinone and hydroquinone forms of Arabidopsis cryptochrome by molecular oxygen. *FEBS Open Bio* **5**, 885–892 (2015).